

Deep neural network CSES-NET and multi-channel feature fusion for Alzheimer's disease diagnosis

Jianping Qiao^{a,*}, Mowen Zhang^{a,1}, Yanling Fan^a, Kunlun Fang^a, Xiuhe Zhao^b, Shengjun Wang^{b,*}, Zhishun Wang^{c,*}

^a Shandong Province Key Laboratory of Medical Physics and Image Processing Technology, School of Physics and Electronics, Shandong Normal University, Jinan 250014, China

^b Department of Neurology, Qilu Hospital of Shandong University, Jinan 250012, China

^c Department of Psychiatry, Columbia University, New York, NY 10032, United States

ARTICLE INFO

Keywords:

Alzheimer's disease
Deep learning
Feature fusion
Genome-wide association study
sMRI

ABSTRACT

Alzheimer's disease (AD) is an irreversible brain disease. The structural Magnetic Resonance Imaging (sMRI) has been widely used in the diagnosis of AD. However, the characteristic information from a single-mode is not comprehensive. In this paper, we proposed a Convolutional-Squeeze-Excitation-Softmax-NET (CSES-NET) deep neural network combined with multi-channel feature fusion for the diagnosis of AD. First, three kinds of features were extracted including patches based on voxel morphology, cortical features based on surface morphology, and radiomics features. Next, the residual network CSES-NET was proposed to extract the deep features from the patch images in which the features were re-scaled in the residual structure in order to fit the correlation between channels. Then, the fused features of the three channels were applied to classify AD/EMCI/LMCI/NC with the fully connected neural network. Finally, radiomics and cortical features were combined with genetic data for genome-wide association study to assess genetic variants. We performed experiments with 1539 subjects from the Alzheimer's Disease Neuroimaging Initiative (ADNI) database. The experimental results verified that the proposed method improved the effectiveness of the model by extracting nonlinear deep features and fusing the multi-channel features. In addition, the genome-wide association study identified multiple risk SNPs loci which were associated with the pathological of AD and contributed to the early prevention and control of AD.

1. Introduction

Alzheimer's disease (AD) is a genetically complex and multifactorial disease that causes neurodegenerative dementia. The pathology of AD is neuronal dysfunction and loss, and even neuronal death, which results from the aggregation of extracellular amyloidogenic fibers, plaques, and intracellular NFTs [1]. Genetic factors play an important role in the development of Alzheimer's disease. Mild cognitive impairment (MCI) is characterized by mild memory impairment which may be a prodromal symptomatic stage of dementia. Early diagnosis of AD remains challenging in the clinical applications.

Different neuroimaging modalities have been used to identify the early diagnosis of AD, such as structural Magnetic Resonance Imaging (sMRI), Electroencephalography (EEG), functional MRI (fMRI), and Diffusion Tensor Imaging (DTI) [2,3,4]. Structural MRI has been widely

developed for feature extraction and diagnostic classification with the traditional machine learning techniques and deep learning-based methods. Generally, the biomarkers extraction methods fall into three main categories: voxel-based morphometry (VBM) methods, radiomics-based methods, and surface-based morphometry (SBM) methods.

The voxel-based morphometry (VBM) approach usually takes the voxels of gray matter images as features [5]. Basher et al. extracted volumetric features from the left and right hippocampus of structural magnetic resonance imaging (sMRI) data and used a CNN model classification approach to diagnose AD [6]. Ahmed et al. selected the hippocampus, amygdala, and insula from sMRI gray matter images and fed Three-view patches (TVPs) of these regions into CNN for training [7]. Zhu et al. proposed a dual-attention multi-instance deep learning network for the early diagnosis of AD and MCI [8], which enhanced the identification of discriminative features.

* Corresponding authors at: School of Physics and Electronics, Shandong Normal University, No.88 Wenhua East Road, Jinan, Shandong 250014, China (J. Qiao).
E-mail addresses: jpqiao@sdu.edu.cn (J. Qiao), junwang9999@sina.com (S. Wang), wangz@nyspi.columbia.edu (Z. Wang).

¹ Co-first authors: Jianping Qiao and Mowen Zhang contributed equally to this work.

The radiomics-based method was an effective method for feature extraction of structural brain lesions [9]. The abnormal hippocampal shape in sMRI was used to predict the transition from MCI to AD with machine learning method [10]. Feng et al. extracted 1692 radiomics features in the caudal and head parts of the bilateral hippocampus and used support vector machines to differentiate AD and NC [11]. The radiomics-based method aimed to mine image features at high throughput to improve diagnostic prediction accuracy.

The surface-based morphometry (SBM) method was also utilized to identify biomarkers of AD [12]. Lahmiri et al. classified AD patients and healthy control subjects with several machine learning classifiers. They extracted surface feature including cerebral cortex, cortical thickness and gyrification index [13]. Wu et al. proposed ROI-based surface morphometry to characterize gray matter degeneration during AD progression [14]. This method demonstrated the sensitivity of multiple cortical indexes for the discrimination of AD, but the small sample size was a major problem. Previous studies focused on cortical thickness instead of sulcus depth and folds.

Genetic factors play an important role in the development of Alzheimer's disease. AD is preceded by a long asymptomatic period during which the proteins in the brain of the affected person have abnormal functions. The diversity of amyloid protein fiber structures is closely related to disease progression. Amyloid plaques may be a trigger or driver of the disease. The accumulation of amyloid in the brain may trigger the complex multicellular neurodegenerative process [15]. Genome-wide association study (GWAS) is a statistical approach to identify single nucleotide polymorphisms (SNPs) associated with phenotypes. The GWAS had been applied in genetic analysis of Alzheimer's disease in which the dichotomous clinical diagnostic status categories were used as phenotypes. In addition, the association of genes with gray matter volume was studied. The hippocampal volume in sMRI imaging was analyzed as type data for Genome-wide association study [16,17]. Nevertheless, most of the GWAS studies neglected the cortical and subcortical surface and radiomics changes which might lead to the ignorance of the causative genes in the cerebral cortex.

In this paper, we proposed a Convolutional-Squeeze-Excitation-Softmax-NET (CSES-NET) based multi-channel Feature Fusion Classification Network to classify AD, NC, Early Mild Cognitive Impairment (EMCI), and Late Mild Cognitive Impairment (LMCI). First, VBM-based patches, SBM-based features, and radiomics-based features were extracted from sMRI. Then, we built the CSES-NET to extract deep features with higher discriminative power in the network channel perspective. Especially, the CSES-NET applied an attention mechanism with feature scaling to the residual structure, which enabled the network to avoid gradient dissipation and extract more nonlinear depth features through interdependence between channels. Finally, the CSES-NET was embedded with the shallow neural classification network for feature fusion of multiple channels and classification of AD, LMCI, EMCI, and NC.

The main contributions of this study were stated as follows: (i) The CSES-MFF-NET model utilized three types of features to characterize the lesion information. The VBM-based features captured the brain regions with structural atrophy, which were extracted by neural networks with nonlinear expression of depth features. The SBM-based features captured the regions with abnormal cortical thickness, folds, cortical complexity and sulcus depth, which were extracted by reconstructing the cerebral cortex based on the thickness of the brain gray matter. The radiomics-based features captured first order statistics, shape and texture, which were extracted from the original image, wavelet transform image, and Gaussian image. The fusion of different features could improve the effectiveness and stability of the model. (ii) The gene data were combined with the neuroimage phenotypic information which indicated the relevant causative genes and potential biomarkers of AD.

2. Materials and methods

2.1. Dataset

The Alzheimer's Disease Neuroimaging Initiative (ADNI) (<https://adni.loni.usc.edu>) was used in this study. We used T1-weighted structural MRI data with 3T scan intensities from the three datasets at baseline. The training set was ADNI-1 and ADNI-2. The test set was ADNI-3 for the independent data, and the duplicate data from the training set were removed from the test set (Table 1). The model used 10-fold cross-validation where all the data in the training set were randomly divided into ten equal parts, one of which was selected as the validation set. The testing set was independent of the training set and validation set.

2.2. Image preprocessing

Preprocessing was performed using the SPM-based Computational Anatomy Toolbox for SPM12 (CAT12) in MATLAB. First, the SPM-display for anterior conjoined (AC)-posterior conjoined (PC) correction was used to remove the head movement bias of the individual when the MR images were scanned. After aligning all images, we removed the skull and excise the cerebellum operation. Then, MR images were denoised, de-biased, T1 global intensity corrected and corrected noise by the non-local mean (NLM) filter. Each MR image was tissue segmented to yield a gray matter GM image. Next, all subject GM images were aligned to the Montreal Neurological Institute (MNI) standard template. Finally, modulation normalization was performed to compensate for the effects of spatial normalization, which caused volume changes due to affine transformation and nonlinear warping. The modulated images retained the total amount of gray matter signal in the normalized partition. Therefore, volume correction was performed on the modulated GM gray matter images.

2.3. Deep features based on CSES-NET

First, we selected the regions of interest (ROIs) with significant differences by the Statistical Parametric Mapping 12 (SPM12) toolbox. Specifically, the GM image generated by segmentation during image preprocessing was smoothed with an 8 mm Gaussian kernel to improve the signal-to-noise ratio of the image data. Then the generalized linear statistical model was developed, which was intended to establish the same two-sample *t*-test statistical model for each voxel. After that, the parameters of the statistical model were estimated and the T-statistic of each voxel was calculated to generate the SPM map. Last, we used the Family Wise Error (FWE) to get the anomalous region at the significant level ($p < 0.01$) and transformed the landmark locations from MNI space coordinates to the space voxel coordinates by using MRICroN software.

Second, the nonoverlapping image patches were extracted according to the center of the significant regions. The group comparisons were conducted between the training set ADNI-1 and ADNI-2 instead of the testing set, which avoided the overfitting of the model. These patches were spliced and used as input images for the CSES-NET channel

Table 1
Demographic information of the subjects.

Dataset	Category	Number	Age (Mean \pm std)	Gender (Male/Female)
ADNI1	AD	197	75.73 \pm 7.71	101/96
	NC	224	76.13 \pm 4.94	118/106
ADNI2	AD	155	74.75 \pm 7.97	89/66
	NC	193	73.34 \pm 6.43	91/103
	EMCI	216	71.11 \pm 6.85	119/97
	LMCI	162	72.36 \pm 7.48	90/72
ADNI3	AD	63	74.67 \pm 7.88	38/25
	NC	329	70.18 \pm 6.37	173/212

attention deep neural network.

Third, we proposed the CSES-NET channel attention residual neural network for the deep feature extraction. This network consisted of sixteen blocks and each block was divided into the convolutional path and the identity path, as shown in Fig. 2. Specifically, the convolutional path was used to change the dimensionality of the network and extract features. The identity path was used to deepen the network. The residual convolution block was utilized to avoid the gradient disappearance which was caused by amounts of layers of the deep learning network. In the proposed CSES-NET network, each convolutional path contained three convolutional layers and channel attention mechanism. Specifically, the average pooling layer was added after the convolutional path to squeeze the feature map. The two connected convolutional layers were used to extract nonlinear features and increase the nonlinear representation of features. Then the softmax layer was activated to obtain the probability number between 0 and 1 to extract the feature importance of each channel. The feature weights were multiplied and summed with the input of this block. The high weights enhanced the highlighted features and suppresses the use less ones. The CSES channel attention model in the deep network provided discriminative deep features for classification.

The deep network consisted of sixteen CSES blocks. In each block, the output of the convolutional block in the backbone network was the input X of the channel attention model. After the convolution block operation, the output U was obtained. Then U passed through the global average pooling layer and completed the squeeze operation, which squeezed the matrix of $H \times W \times C$ to $1 \times 1 \times C$. The information of each channel was represented by the global average pooling value of the channel. Then we could get U_s by:

$$U_s = F_{sq}(U) = \frac{1}{W \times H} \sum_{i=1}^W \sum_{j=1}^H U(i,j) \quad (1)$$

where U_s passed through two 2D convolutional layers with a convolutional kernel size of 1×1 . The channel number of the two convolution layers were $\frac{C}{16}$ and C , respectively. The depth nonlinear characteristic U_e was computed by:

$$U_e = F_{ex}(U_s) = W_2 \delta(W_1 U_s) \quad (2)$$

where δ represented the ReLU activation function, $W_1 \in R^{C \times C}$ and

$W_2 \in R^{C \times \frac{C}{16}}$. Let σ denoted the softmax function, the probability value U_y was obtained by scaling U_e which was expressed by:

$$U_y = F_{sm}(U_e) = \sigma(W_2 \delta(W_1 U_s)) \quad (3)$$

The final output Y of the CSES module was obtained by:

$$Y = I + I^* U_y \quad (4)$$

This weight U_y enhanced useful features and suppressed useless features which improved the judgment ability of the network by increasing the weight of the effective profile map. The depth network was generated by the superposition of CSES channel attention modules, which gradually dominated the entire depth network and weakened the weight of useless features. Therefore, the proposed CSES block provided discriminating deep feature for the classification.

2.4. Radiomics-based features

We used the pyradiomics package which was an open-source Python toolkit to extract radiomics features. Radiomics features were generated from the original image, wavelet filtered image and Laplace Gaussian (LoG) filtered image. The wavelet filter was applied to the original image to obtain the decomposed and approximated images. The Laplace Gaussian filter was used as an edge enhancement filter. The shape, intensity, and texture features included First Order features, Shape features (3D), Shape features (2D), Gray Level Co-occurrence Matrix (GLCM) features, Gray Level Size Zone Matrix (GLSZM) features, Gray Level Run Length Matrix (GLRLM) features, Neighbouring Gray Tone Difference Matrix (NGTDM) features, Gray Level Dependence Matrix (GLDM) features. Then the feature selection was performed by using LightGBM with the 1291 extracted radiomics features. Specifically, the left-wise strategy was used to select the node with the greatest divergence benefit from all the current leaf nodes for splitting. Finally, the features with significant heterogeneity were selected for classification.

2.5. Surface morphological features

The surface-based morphometric method was used to extract cortical surface features. In the preprocessing stage, all samples were subjected to the anterior concatenation-posterior concatenation (AC-PC) correction to eliminate head movement bias in individuals scanning MR

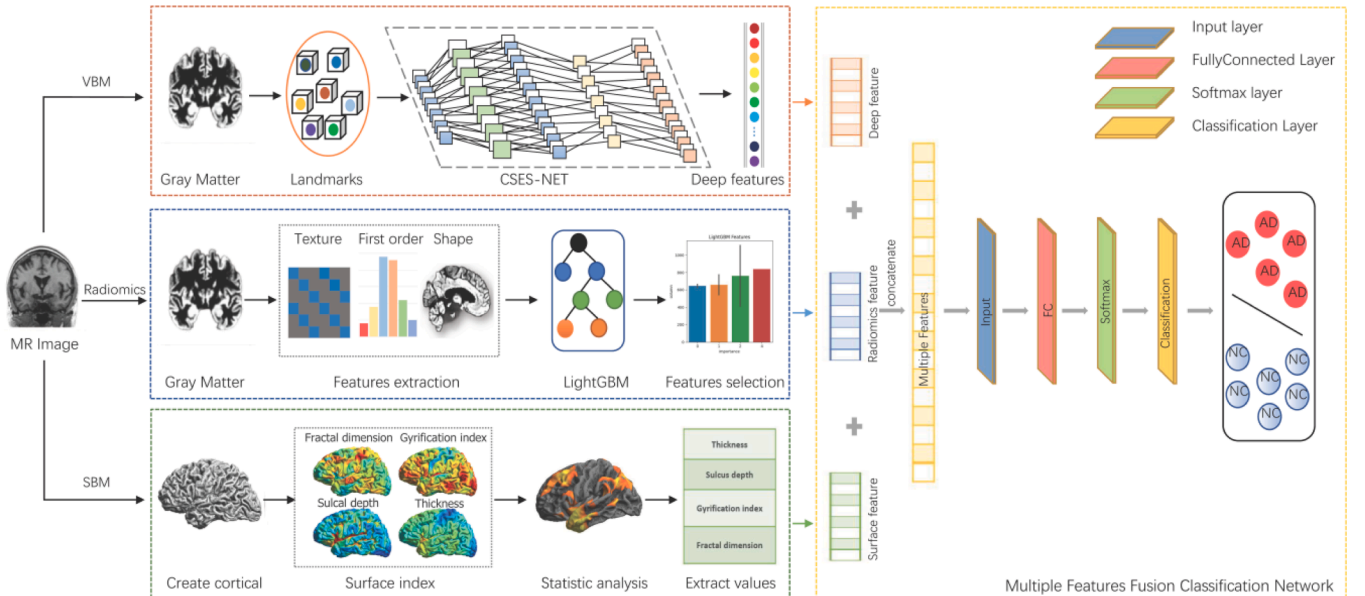


Fig. 1. The framework of the Alzheimer's disease classification algorithm based on the Convolutional-Squeeze-Excitation-Softmax Multi-channel Feature Fusion Classification Network (CSES-MFF-NET).

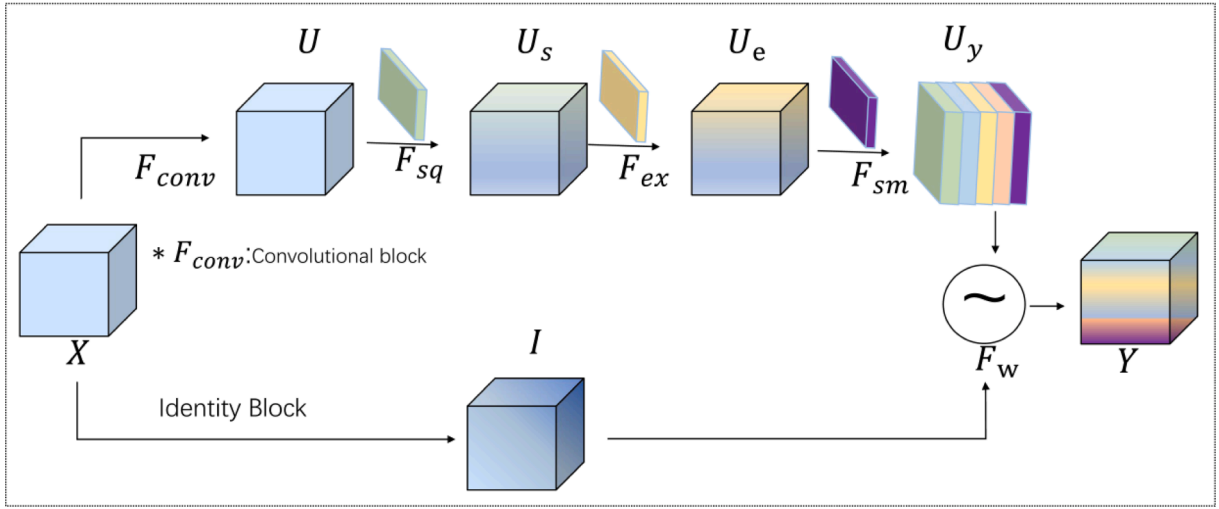


Fig. 2. Convolutional-Squeeze-Excitation-Softmax block.

images. We implemented skull removal, cerebellar excision operations, global intensity correction, intensity normalized denoising and local adaptive segmentation using CAT12 after manual alignment of all images. Creation of initial surfaces was performed in the left and right cerebral hemispheres including topology correction and surface refinement, refinement of central surface correction in the highly collapsed region of the central surface, spherical mapping with area smoothing and reconstruction of the cortical surface.

We calculated the cortical thickness, sulcus depth, gyrification index and fractal dimension of each ROI based on brain mapping templates “DK40”, “HCP_MMP1” and “a2009s”. Then all data of each sample were concatenated into a 1×2344 row vector. The feature selection of the cortical indexes was performed using LightGBM to obtain the features that contribute to the classification.

2.6. Multi-channel feature fusion and classification

The framework of multi-channel feature fusion classification network (CSES-MFF-NET) was shown in Fig. 1. First, the selected radiomics features and cortical index features were normalized to match the numerical distribution of the deep features. Then, the normalized radiomics features and cortical features were connected with discriminative depth features to form a $1 \times m_1$ column vector. The vector was inputted into a five-layer neural network with the input layer, two fully connected layers, softmax layer and classification layer. The non-linear representation of the feature data was obtained through the connected layers. Finally, the softmax layer and the classification layer were used to make the final classification prediction.

The concatenated feature column vector was used as the input of the classification network :

$$F = [F_1, F_2, \dots, F_m]^T \quad (5)$$

After the two fully connected layers, the local feature values were integrated to form the feature map :

$$X = W_2(W_1F + b_1) + b_2 \quad (6)$$

where $X \in [a_1, a_2]^T$, m_1 and m_2 were the number of channels, $W_1 \in R^{m_1 \times m_2}$, $W_2 \in R^{m_2 \times m_3}$, $b_1 \in R^{m_2}$, $b_2 \in R^{m_3}$. The output of the model was compressed into the (0,1) interval by using the Softmax function to obtain the probability of the model which was used to judge whether the sample to be the positive or negative classes S_j :

$$S_j = \frac{e^{a_j}}{\sum_{i=1}^T e^{a_i}} \quad (7)$$

where T means class number. The final category of the sample was determined by the largest value in the probability S_j .

2.7. Genome-wide association study

The genetic data of the 651 subjects which were conducted in the SMRI analysis from both ADNI1 and ADNI2 datasets were utilized for genome-wide association study. First, we pre-analyzed the features obtained from the CSES-MFF-NET by using Statistical Product and Service Solutions (SPSS). The data analysis was conducted on the features with large classification contribution values after the selection of radiomics features and cortical index features. Significance analysis was conducted for each characteristic value by using the independent sample *t*-test in SPSS software. Then features with significance $p < 0.01$ were reserved for correlation analysis of phenotypic information. After that, quality control (QC) was performed with the following eight steps:

- (1) The genetic data and phenotypic data of the two databases were combined to get a total of 1,008,823 SNPs loci and 1550 subject samples.
- (2) Subjects were screened for stringent deletion rates. Subjects with locus deletion rates and individual deletion rates of more than 0.02 were removed.
- (3) Subjects were screened by Minimum Allele Frequency (MAF) method. The SNPs with $MAF < 0.05$ were removed to avoid false positives, which corresponded to the same gene and contributed less information. Therefore, the 300,360 variants and 1526 people were selected for the next steps.
- (4) The Hardy-Weinberg Equilibrium (HWE) was the law of genetic equilibrium. The frequency of each genotype was calculated by:

$$(p + q)^2 = p^2 + 2pq + q^2 \quad (8)$$

where $p + q = 1$, $(p + q)^2 = 1$. The expected value E was obtained for each genotype, and the number of observations A was compared with the expected value E by χ^2 test:

$$\chi^2 = \sum \frac{(A - E)^2}{E} \quad (9)$$

The 299,167 SNPs and 1526 individuals with genetic susceptibility greater than 0.000001 were retained by the chi-square test.

- (5) The Heterozygosity test was used for SNPs selection. The frequency of heterozygous genotypes HET for each subject was calculated by:

$$HET = (NM - HOM)/NM \quad (10)$$

where the number of pure genotypes per subject was denoted by HOM and the total number of genotypes was denoted by NM . Individuals with high or low heterozygosity and sample heterozygosity deviating from ± 3 standard deviations from the mean were excluded. The lower and upper bounds of the HET values were expressed by:

$$min = mean(HET) + 3*std(HET) \quad (11)$$

$$max = mean(HET) - 3*std(HET) \quad (12)$$

We selected 1486 individuals with HET values within the boundary.

- (6) Linkage disequilibrium (LD) screening SNPs was used to measure whether genotypic changes in two molecular markers were synchronized and correlated. The LD was computed by using the correlation coefficient r^2 :

$$r^2 = \frac{D^2}{p_A(1-p_A)p_B(1-p_B)} \quad (13)$$

where D was the coefficient of linkage disequilibrium, p_A was the frequency of the A gene line in the allele, p_B was the frequency of B genotype. We excluded SNPs with correlation coefficients greater than 0.5 which were not completely independently inherited during inheritance. The 187,622 independent SNPs were selected.

- (7) We used principal component analysis (PCA) to estimate genetic background covariance which was used to adjust tests of association. We completed the correction of population stratification phenomenon to avoid spurious association due to population stratification.
- (8) Phenotypic information filtering. The 620 subjects with both genetic and phenotypic information were retained.

The 187,622 variants and 620 people were selected after the quality control process. We utilized the radiomics features and cortical metrics that were statistically significantly different ($p < 0.01$) for the early classification of AD for association analysis. Genome-wide association analysis was conducted sequentially with eight radiomics features and fourteen vertex cortical indexes.

3. Results

3.1. Evaluation metrics

The accuracy (ACC), sensitivity (SEN), specificity (SPE), precision (PRE), recall (REC), F1 score, and Area Under Curve (AUC) were used as evaluation metrics to evaluate the performance of the model. The performance was further visualized using ROC curves for comparison. The TP denoted true positive, TN denoted true negative, FP denoted false positive, and FN denoted false negative. The accuracy was the percentage of correct predictions for all samples to the total sample. Sensitivity indicated the percentage of all patients that were predicted correctly and measured the ability of the classifier to identify patients. Specificity was similar to sensitivity and measured the ability of the model to identify normal controls. Precision meant the probability of actual disease in the population judged to be diseased. Recall meant the average of both categories being predicted correctly. F1score was used for comprehensive evaluation.

3.2. Methods for comparison

The proposed method was compared with four classification models which were (i) Resnet method [18]. The Resnet50 deep residual network was directly applied to classify subjects. (ii) CSES-NET method [19]. Deep neural networks containing attention mechanisms were used for

feature extraction. The final predictive classification was performed by two fully connected layers and a softmax layer. (iii) CSES-SVM method [20]. Features were extracted from deep neural networks and support vector machines was used as classifier. (iv) CSES-MFF-SVM method [21]. The deep features were extracted with the deep neural network. The radiomics and cortical features were spliced with the deep features. The SVM was used for classification. The same input images were applied in all comparison experiments.

3.3. Classification results

The brain voxel and surface comparisons identified significantly different regions between AD and NC which were shown in Fig. 3 and Fig. 4. The anatomical landmarks were used as biomarkers and the prediction of AD.

The Table 2 showed the results of AD, NC, EMCI, and LMCI classification of different models. The ACC and AUC of the proposed CSES-MFF-NET method were better than other classification models. The accuracy of AD and NC classification was 96.17%. The SEN, SPE, PRE, RECALL, F1 score and AUC were 84.13%, 98.48%, 94.19%, 91.30%, 92.73% and 98.83%, respectively. The ROC curves of the different classification models were shown in Fig. 5. The proposed CSES-MFF-NET method had higher evaluation indexes compared with existing methods.

We also compared the proposed CSES-MFF-NET method for AD/NC classification with other state-of-the-art methods with the same datasets, including (i) the method using landmark blocks with convolutional neural networks [22,23], (ii) the method combining radiomics features with SVM [24], (iii) the landmark blocks using residual network dense net classification [25], (iv) the method based on ROI region block features combined with Linear Discriminant Analysis (LDA) [26], (v) the method of convolutional network for classification of hippocampal image blocks in ROI region [27], (vi) dual attention multi-instance deep learning [8], (vii) the method of multiple feature fusion based on ROI [28]. The comparison results were shown in Table 3. The proposed method outperformed other advanced methods in terms of accuracy, SEN, SPE and AUC results.

In addition, Table 4 showed the comparison results of the EMCI/LMCI classification. The comparison methods included (i) MRI and DTI multimodal ROI image blocks [26], (ii) brain functional connectivity networks and sparse matrices [29], (iii) brain connectivity networks combined with SVM [30], (iv) DWI diffusion-weighted imaging of brain network structures [31], (v) shape features and multilayer perceptron (MLP) based classification method [32]. The experimental results demonstrated that the proposed CSES-MFF-NET method had the best performance for EMCI/LMCI classification.

3.4. GWAS results

We selected eight radiomics features and cortical thickness features in fourteen brain regions by using the significance analysis with p -values < 0.01 . The radiomics and surface features were extracted from the multi-channel feature fusion framework. These feature values were used as phenotypic information for association analysis to obtain the associated SNPs loci and risk genes. The Manhattan plots of analysis result were shown in Fig. 6. Specifically, rs162031 was correlated with two radiomics features which were log-sigma-3-0-mm-3D_glszm_GLN and wavelet-LLL_glszm_SZN. Moreover, the rs10801929, rs12565115, rs2075650 and rs2225612 were associated with cortical thickness in multiple brain regions. Three SNPs were significantly correlated ($p < 1 \times 10^{-6}$) with the wavelet-LLL_glszm_SZN and the thickness of two brain regions. The Hamanton and Quantile-Quantile (Q-Q) plot of three phenotypic information were presented as shown in Fig. 7. The specific information of all SNPs loci with significance was shown in Table 5, in which several risk loci were associated with abnormalities in brain

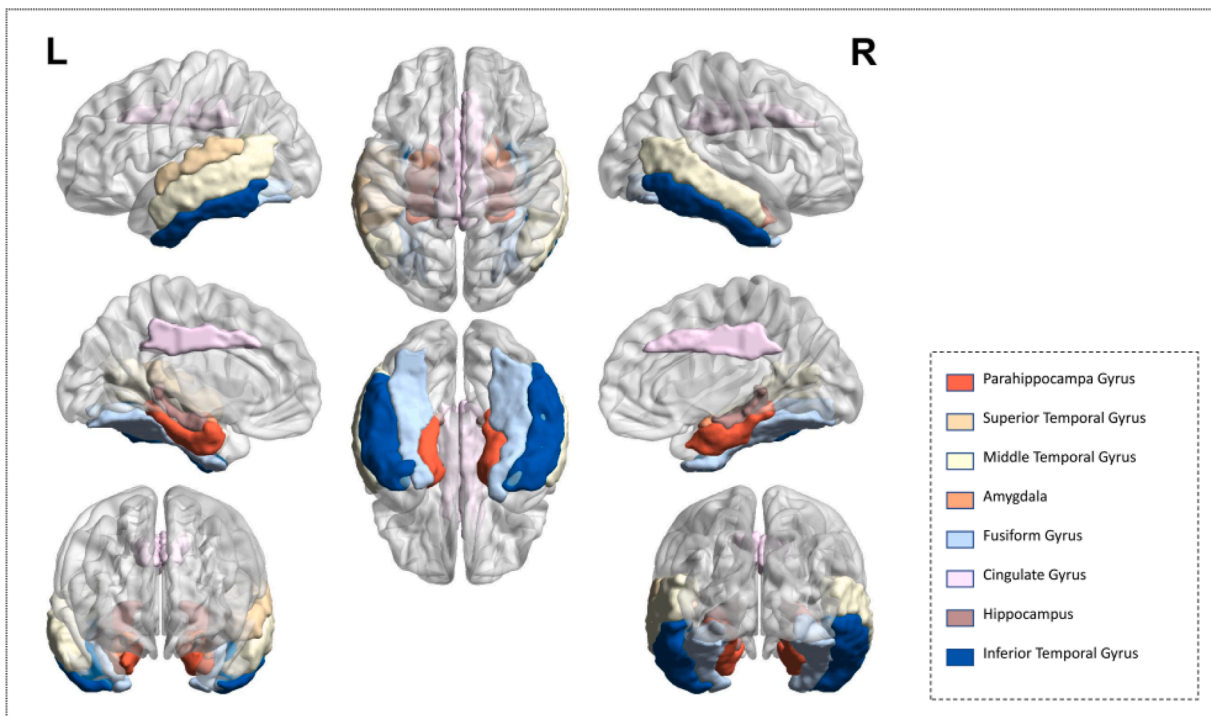


Fig. 3. Visualization of differential brain regions for comparison between groups based on VBM.

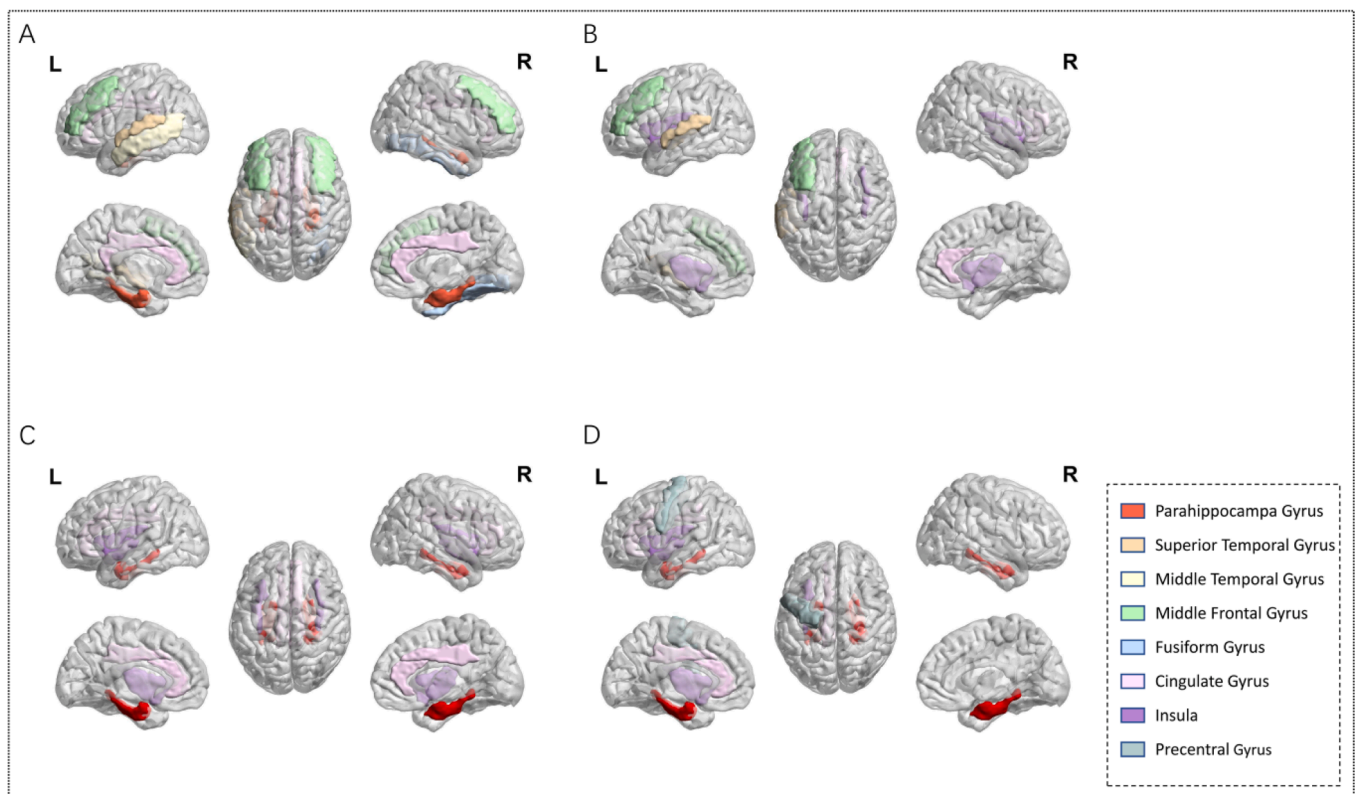


Fig. 4. Visualizations of brain regions with significant differences in cortical indicators based on SBM.

structure or neuroproteins. The proposed method used brain imaging as the dependent variable and identified genes that influenced brain imaging differences between AD and NC.

4. Discussion

We proposed the Convolutional-Squeeze-Excitation-Softmax-NET (CSES-NET) deep neural network combined with the multi-channel feature fusion method for AD, NC, EMCI, and LMCI classification. In

Table 2
Classification results of the proposed method and the comparison methods.

Method	Classification													
	AD/NC							AD/LMCI						
	ACC	SEN	SPE	P	R	F1	AUC	ACC	SEN	SPE	P	R	F1	AUC
Resnet	0.923	0.698	0.966	0.871	0.832	0.861	0.923	0.781	0.8571	0.583	0.726	0.720	0.7273	0.810
CSES-SVM	0.938	0.809	0.963	0.886	0.886	0.886	0.971	0.839	0.8730	0.750	0.797	0.797	0.8042	0.881
CSES-NET	0.941	0.821	0.960	0.886	0.901	0.893	0.971	0.850	0.8889	0.750	0.811	0.811	0.8155	0.884
CSES-MFF-SVM	0.946	0.841	0.966	0.898	0.903	0.901	0.973	0.862	0.9048	0.767	0.810	0.810	0.8211	0.888
CSES-MFF-NET	0.962	0.841	0.985	0.942	0.913	0.927	0.988	0.874	0.9365	0.792	0.840	0.840	0.8293	0.892
Method	Classification													
	EMCI/LMCI							NC/LMCI						
	ACC	SEN	SPE	P	R	F1	AUC	ACC	SEN	SPE	P	R	F1	AUC
Resnet	0.631	0.520	0.686	0.597	0.603	0.599	0.629	0.747	0.108	0.9524	0.6922	0.580	0.631	0.678
CSES-SVM	0.658	0.622	0.771	0.627	0.618	0.622	0.635	0.816	0.500	0.9365	0.7905	0.718	0.752	0.804
CSES-NET	0.671	0.464	0.792	0.641	0.628	0.635	0.641	0.816	0.500	0.9365	0.7905	0.718	0.752	0.803
CSES-MFF-SVM	0.644	0.464	0.750	0.613	0.607	0.610	0.636	0.839	0.500	0.9841	0.8464	0.742	0.984	0.803
CSES-MFF-NET	0.724	0.714	0.729	0.710	0.722	0.716	0.775	0.851	0.500	0.985	0.881	0.734	0.968	0.804
Method	Classification													
	NC/EMCI							AD/EMCI						
	ACC	SEN	SPE	P	R	F1	AUC	ACC	SEN	SPE	P	R	F1	AUC
Resnet	0.642	0.506	0.762	0.590	0.584	0.587	0.715	0.863	0.921	0.750	0.853	0.835	0.844	0.903
CSES-SVM	0.695	0.656	0.762	0.671	0.685	0.678	0.719	0.874	0.921	0.781	0.862	0.851	0.857	0.919
CSES-NET	0.726	0.594	0.793	0.697	0.694	0.694	0.725	0.884	0.937	0.781	0.878	0.859	0.868	0.918
CSES-MFF-SVM	0.697	0.625	0.730	0.667	0.678	0.672	0.723	0.884	0.936	0.781	0.878	0.859	0.868	0.921
CSES-MFF-NET	0.737	0.656	0.857	0.726	0.677	0.694	0.760	0.895	0.952	0.781	0.894	0.867	0.880	0.926

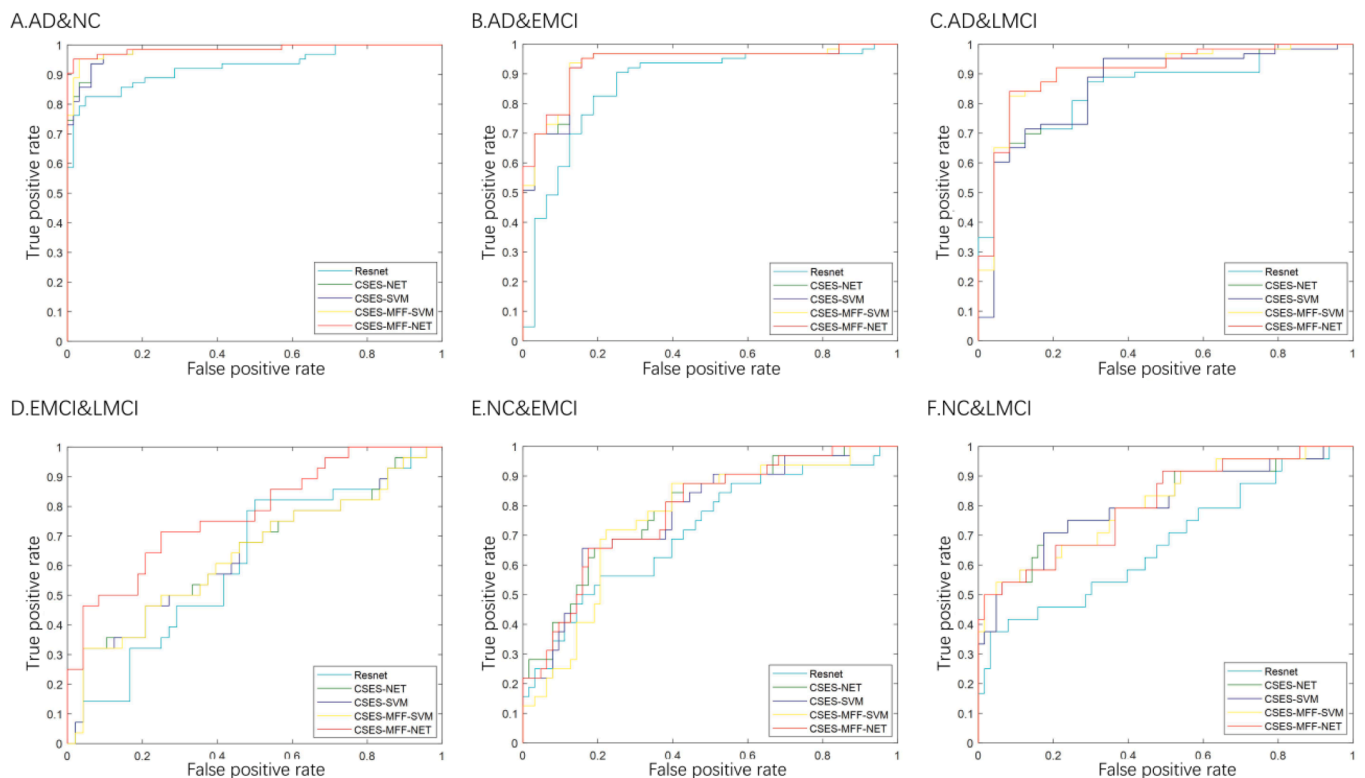


Fig. 5. ROC curves for the comparison of the five methods of AD/EMCI/LMCI/NC classification.

addition, the genetic data combined with radiomics features and cortical metrics were analyzed to obtain the associated SNPs loci and risk genes by utilizing the genome-wide association study. We found several risk genes associated with phenotypic features and analyzed the role of gene function on traits.

The landmark regions based on VBM and SBM were consistent with the previous studies[33]. We found the significant differences in the

hippocampus, amygdala, thalamus, cingulum, and fusiform gyrus in AD by using the gray matter images with VBM. Moreover, we performed the group comparison of the cortical thickness, sulcus depth, gyrification index and fractal dimension of the cortex with surface-based morphology method. These results could be stated as follows. First, the thickness of AD had significant atrophic changes in brain regions such as bilateral parahippocampal gyrus, left superior temporal gyrus,

Table 3

AD/NC: Performance comparison of the proposed method with the state-of-the-art methods.

Reference	Method	ACC	SEN	SPE	AUC
Liu et al. [22]	patch + CNN	0.9056	0.8742	0.9303	0.9574
Wu et al. [24]	Radiomics + SVM	0.8903	0.8544	0.9197	0.9110
Li et al. [25]	Landmark patch + Densenet	0.8950	0.8790	0.9080	0.9240
Lian et al. [23]	patch + CNN	0.9030	0.8240	0.9650	0.9510
Zhu et al. [8]	patch + DCNN	0.9240	0.9100	0.9380	0.9650
Liu et al. [26]	Multi ROI feature + SVM ensemble	0.9465	0.8889	0.9503	0.9826
Hett et al. [26]	ROI patch + LDA	0.9130	0.9340	0.8300	0.9470
Cui et al. [27]	ROI patch + CNN	0.9229	0.9063	0.9372	0.9695
CSES-MFF-NET(ours)	Multi-feature fusion + CNN	0.9617	0.8413	0.9848	0.9883

Table 4

EMCI/LMCI: Performance comparison of the proposed method with the state-of-the-art methods.

Reference	Method	EMCI/LMCI	ACC	SEN	SPE	AUC
Hett et al. [26]	ROI patch	65/34	0.688	–	–	0.661
Zhan et al. [29]	Connectivity network	73/39	0.650	0.78	0.64	0.70
Prasad et al. [30]	Connectivity network	74/38	0.634	–	–	–
La Rocca et al. [31]	network features	85/38	0.700	0.76	0.65	0.70
Shakeri et al. [32]	Shape feature	160/160	0.630	0.620	0.660	–
CSES-MFF-NET(ours)	Multi-feature fusion	216/162	0.7237	0.7143	0.7292	0.7753

left middle temporal gyrus, right fusiform gyrus, bilateral middle frontal gyrus and bilateral cingulate gyrus, as shown in Fig. 4 (A). Second, there were significant differences of the sulcus depth indexes in the right anterior gyrus, left middle frontal gyrus, left superior temporal gyrus and both insula, as shown in Fig. 4(B). Third, the gyrification index had significant differences in the parahippocampal gyrus, insula and right cingulate gyrus, as shown in Fig. 4(C). Finally, fractal dimension of the left precentral gyrus, left insula, left cingulate gyrus and both parahippocampal gyrus changed significantly, as shown in Fig. 4(D). These findings were consistent with the previous studies including VBM analysis, medical clinical experience and cortical thickness. [34,35]. Specifically, the thickness in the temporal and frontal lobes was thinned in patients with diseases from mild cognitive impairment to Alzheimer’s disease, which was highly coincident in the VBM and SBM group comparison analysis. Therefore, there was correlation between SBM cortical changes and VBM gray voxel strength differences, both of which might be used as biomarkers for AD diagnosis. These results indicated the heterogeneity in the changes of brain tissue and clinical outcomes of individuals with AD.

We conducted the VBM and SBM analysis as well as the group comparison between AD and NC. Consistent with the previous studies [33–35], we found gray matter atrophy and cortical thinning in the brain regions including hippocampus, amygdala, thalamus, cingulum and fusiform gyrus in AD compared with NC, which may be related to the memory, emotion, attention and cognition disorder of the patients. These findings of the abnormal brain areas were used as the biomarkers in the classification models which might be helpful for the pathology and treatment of AD such as Transcranial Magnetic Stimulation (TMS) [36]. TMS was used to alter the action potential of cortical neurons by changing the induced current in the cerebral cortex, which in turn affected the metabolism of substances and neurophysiological activity in the brain [37]. The precise abnormal brain regions would benefit the TMS treatment and help slow down the progression of the patient’s disease.

The proposed channel attention deep learning networks for early diagnosis of AD had the better performance in comparison with various advanced methods. Shakeri et al. used a softmax-activated multilayer perceptron for hippocampal shape features in the somatic part to identify AD [32]. Salunkhe et al. captured the texture features of the region of interest based grayscale symbiotic matrix (GLCM) for AD

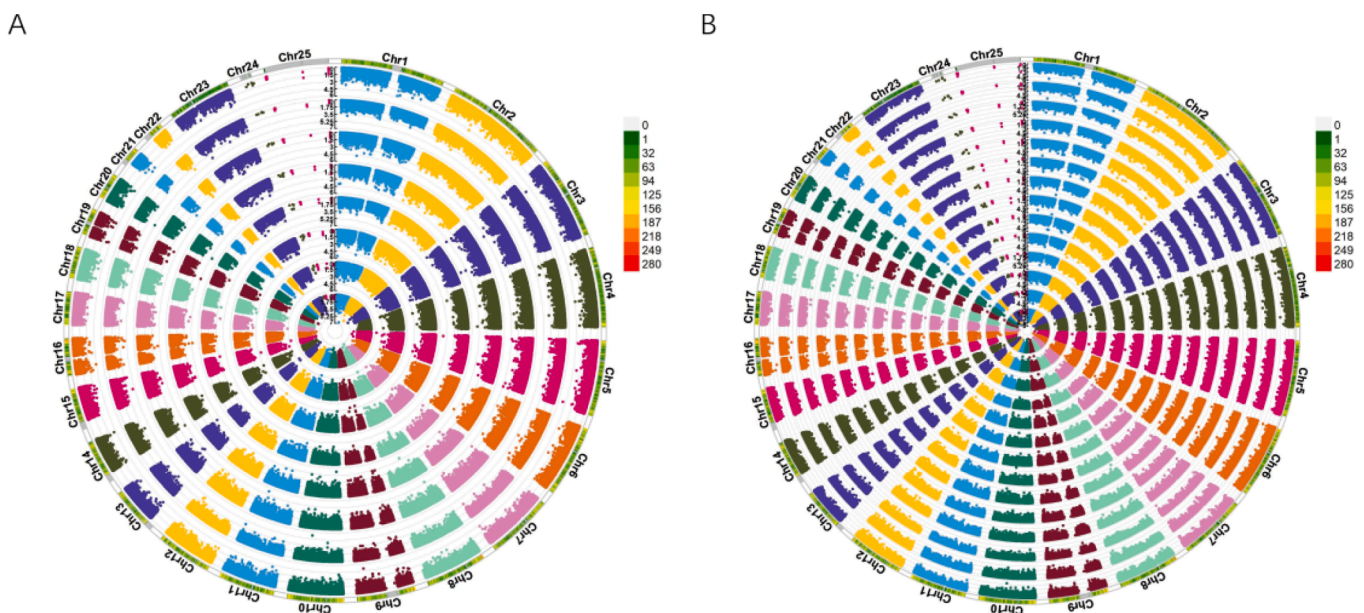


Fig. 6. Presentation of the results of the association analysis: (A) Ring Manhattan plot of 8 radiomics features significantly associated with the presence or absence of disease (B) Ring Manhattan plot of 14 cortical index features significantly associated with the presence or absence of disease.

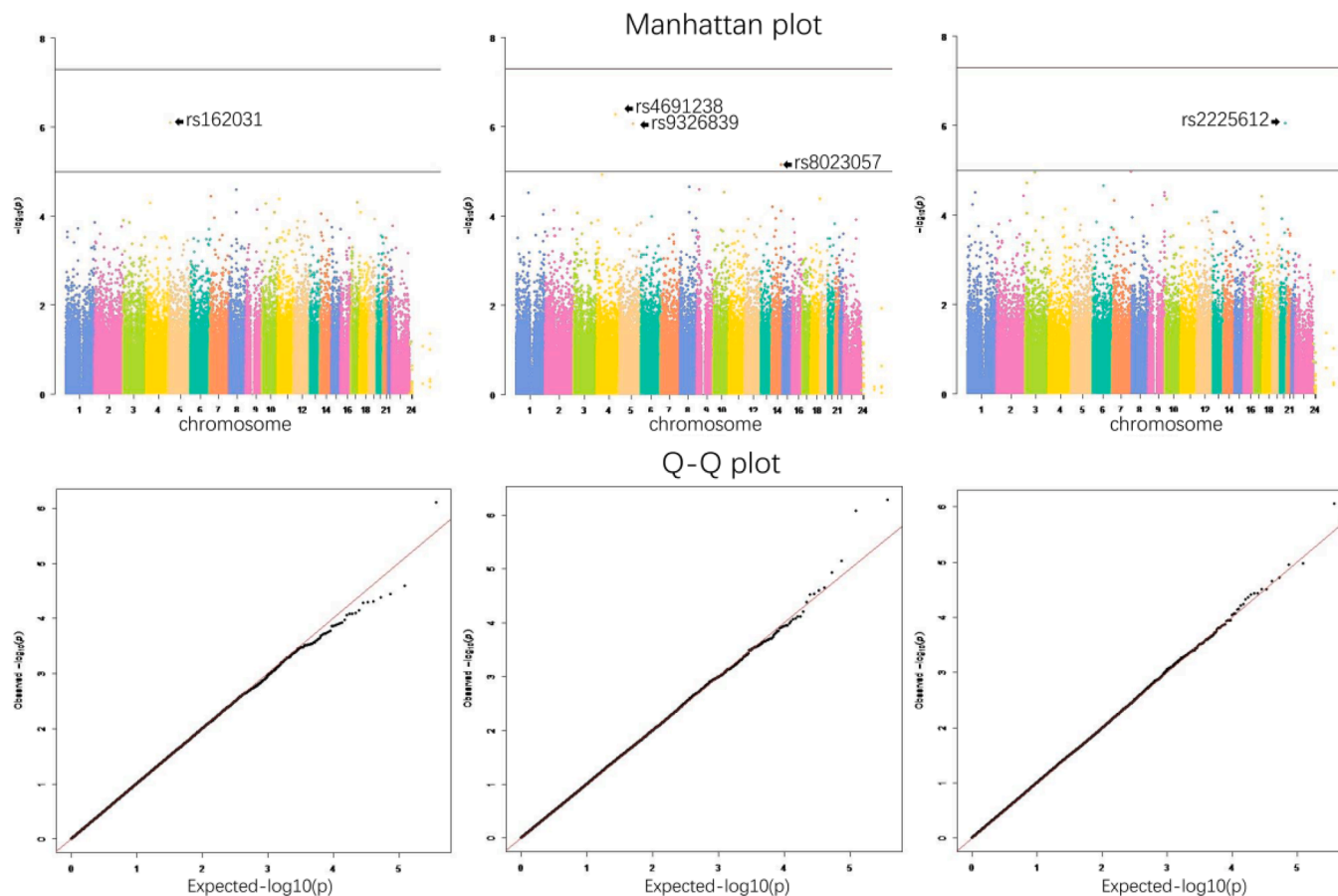


Fig. 7. Manhattan and Q-Q plots for association analysis of three significantly correlated phenotypic features (the results of the analysis of Precentral gyrus thickness, Posterior Orbital Frontal Complex thickness, and wavelet-LLL_glszm_SZN textural feature are shown from left to right, with significant SNPs marked).

classification [38]. However, most researchers used traditional machine learning methods to classify shallow and low-dimensional features, such as shape, texture, first-order statistics and cortical metrics. In this study, we attempted to combine multiple features with channel attention deep learning networks. According to the comparative experiment with the SVM method, the proposed fully connected classification network had slight advantages. Hett et al. combined structural and diffusion MRI based on the framework of the multimodal patch to improve the performance of the current hippocampus-based classification [26]. The fusion of the multimodality might be benefit for the AD and MCI prediction. However, some modalities might be absent during image acquisition which would affect the implementation of these methods [39]. Therefore, the proposed method proceeded to multi-channel features from MRI-based of brain imaging data which achieved better classification results and obtained more pathological information.

In this study, the structural MRI combined with deep-learning methods were used for computer-aided diagnosis of AD. Structural MRI was performed on the MRI scanner and the participants were instructed to rest during scanning. The clinical examinations include plasma markers, biochemical metabolism examination in cerebrospinal fluid, cognitive function test and medical imaging. The accuracy of clinical diagnosis is around 70 % or less [40,41]. Cognitive function was related with AD, but it cannot reflect AD directly because of the individual heterogeneity in experiences and symptomology [42]. The definite diagnosis of AD relied on pathological examination of brain tissue. But the pathological method diagnosis could only be made by examining brain tissue after death. Therefore, this study could find the potential biomarkers and discriminative brain regions associated with the disease, which may help physicians to make accurate diagnosis. In addition, the potential model accuracy improvement and big data would be benefit

for the personalized accurate diagnosis and treatment. The quantification of cortical thickness and sulcus depth for brain regions might be useful for the individualized recommended dosage or evaluating the therapeutic effects of medications. Moreover, the biomarkers had an important role in the drug development process and potential applications in clinical trials. For example, the biomarkers might be used as diagnostic aids to enrich the patient sample with cases of Alzheimer's disease as well as safety markers to detect potential side effects of the drug.

The National Institute on Aging and the Alzheimer's Association (NIA-AA) presented revised diagnostic guidelines for the clinical diagnosis of Alzheimer's disease at the Alzheimer's Association International Conference (AAIC) 2023 (<https://aaic.alz.org/nia-aa.asp>). The biomarkers were grouped into three categories, including core AD biomarkers, non-specific biomarkers and biomarkers of common non-AD co-pathologies. The biomarkers that measured in the anatomic MR imaging in this study were the non-specific biomarkers of tissue reaction involved in AD pathophysiology, which could be used for staging, prognosis and as indicators of biological treatment effect as well as the identification of co-pathology. In addition, imaging and fluid biomarkers within a pathological category were not interchangeable for many use cases. Therefore, the future work will incorporate the imaging and fluid biomarkers in order to define neurodegenerative diseases biologically for AD disease rather than based on syndromic presentation.

Genetics was combined with imaging manifestations of brain diseases to find root-related causes of lesions in brain tissue structures. The GWAS method was used to identify genetic loci associated with traits and identified functional variants and genes. In this study, we found several SNPs and their corresponding genes which were strongly correlated with cortical thickness and texture traits as shown in Table 4.

Table 5
Results of Genome-Wide Association Study of radiomics features and cortical indicators as phenotypic information.

Pheno	SNPs	BP	A1	BETA	STAT	P	Gene	Ch
Thickness7(Somatosensory and Motor Cortex)	rs12565115	39941174	T	0.1031	4.458	9.83E-06	HPCAL4	1
Thickness8(Paracentral lobule and sulcus)	rs10801929	117395987	A	-0.07453	-4.55	6.49E-06	CD101	1
Thickness10(Precentral gyrus)	rs10801929	117395987	A	-0.07157	-4.594	5.29E-06	CD101	1
Thickness13(Primary motor cortex)	rs12565115	39941174	T	0.1377	4.626	4.57E-06	HPCAL4	1
Thickness14(Paracentral lobule and sulcus)	rs12565115	39941174	T	0.1006	4.721	2.92E-06	HPCAL4	1
Thickness14(Paracentral lobule and sulcus)	rs10801929	117395987	A	-0.08547	-4.761	2.42E-06	CD101	1
log-sigma-5 mm-4D_glrml_LRE	rs9866738	31683747	T	-1.277	-4.763	2.39E-06	OSBPL10	3
log-sigma-1 mm-3D_glszm_SALGLE	rs1025192	156310481	T	-0.01293	-4.79	2.10E-06	MME	3
Thickness9(ParaHippocampal)	rs17799799	56663428	G	0.09132	4.472	9.24E-06	CRACD	4
Thickness11(Postcentral gyrus)	rs1203764	2407088	T	0.04773	4.669	3.73E-06	CFAP99	4
log-sigma-5 mm-3D_glrml_LRE	rs12515660	168553502	A	-2.146	-4.471	9.31E-06	SLIT3	5
Thickness4(Posterior orbital frontal complex)	rs9326839	110982999	C	-0.1262	-4.976	8.47E-07	STARD4	5
waveletLLL_glszm_SZN	rs162031	7933287	T	10.03	4.987	8.03E-07	MTRR	5
log-sigma-3 mm-3D_glszm_GLN	rs162031	7933287	T	-14.59	-4.797	2.03E-06	MTRR	5
Thickness1(Circular sulcus of the insula)	rs12199222	17807301	T	-0.07436	-4.567	6.00E-06	NUP153	6
Thickness5(Somatosensory and Motor Cortex)	rs9403008	139194398	T	0.09041	4.693	3.33E-06	ECT2L	6
Thickness9(ParaHippocampal)	rs7823866	14722890	C	-0.123	-4.503	8.03E-06	SGCZ	8
Thickness3(Primary motor cortex)	rs4879382	29781410	A	0.09045	4.509	7.80E-06	PDK1P1	9
Thickness5(Somatosensory and Motor Cortex)	rs10993877	135818892	C	0.04419	4.734	2.74E-06	VAV2	9
log-sigma-1 mm-4D_glszm_SIALGLE	rs2895596	14306091	A	0.0171	4.583	5.58E-06	FRMD4A	10
Thickness8(Paracentral lobule and sulcus)	rs10999463	72101608	A	-0.08242	-4.876	1.38E-06	PRF1	10
Thickness4(Posterior orbital frontal complex)	rs8023057	94167309	G	-0.1142	-4.528	7.16E-06	SERPINA3	14
Thickness5(Somatosensory and Motor Cortex)	rs11160653	19969016	T	-0.04949	-4.631	4.45E-06	KLHL33	14
Thickness2(Central sulcus)	rs2075650	50087459	G	-0.11	-4.625	4.58E-06	TOMM40	19
Thickness3(Primary motor cortex)	rs2075650	50087459	G	-0.0623	-4.637	4.32E-06	TOMM40	19
Thickness3(Primary motor cortex)	rs2225612	44990743	A	-0.0975	-4.966	8.91E-07	EYA2	20
Thickness10(Precentral gyrus)	rs2225612	44990743	A	-0.09414	-4.497	8.25E-06	EYA2	20
log-sigma-4 mm-4D_glszm_GLNN	rs8113842	7860083	A	-0.00579	-4.568	5.97E-06	HAO1	20
Thickness12(Precentral gyrus)	rs2225612	44990743	A	-0.1	-4.784	2.16E-06	EYA2	20
Thickness13(Primary motor cortex)	rs2225612	44990743	A	-0.07286	-4.87	1.42E-06	EYA2	20

Note: Pheno is the characteristic name phenotype (where the thickness information includes the name of the brain region of this ROI in its corresponding brain atlas), SNPs is the RS number, BP (base-pair) is the physical position of the SNPs, A1 is the minor allele name based on the whole sample, NMISS is the number of non-missing genotypes, BETA is regression coefficient, STAT is coefficient t-statistic, P-value is the asymptotic p-value for t-statistic, GENE is implicated gene, Ch indicates the chromosome number of the SNPs.

Risk genes were identified by analyzing the correlation between variants and imaging features of brain abnormal areas. The underlying cause of this correlation was the functional changes in the proteins expressed. Specifically, STARD4 affected specific functions of cellular cholesterol homeostasis in a cell-type-specific manner in the central nervous system. The neurosteroids affected brain cholesterol metabolism, which in turn affected the patient's cognition and behavior [43]. The MME was able to cleave the protease of β -amyloid (β) polypeptide produced by neuronal cells of AD patients. SLIT3 expression caused atrophy of the hippocampus. Variants in the MTRR gene were associated with cognitive impairment, brain atrophy and white matter disease. These brain changes could increase the risk of cognitive impairment and severity of dementia [44]. The FRMD4A could regulate Tau protein secretion through presynaptic vesicle mechanisms and polar signaling pathways. Tau protein release was associated with neuronal activity. Genetic factors affected presynaptic vesicle release in the aging brain, which might influence the progression of AD [45]. It had been reported that SERPINA3 might bound to amyloid. SerpinA3 signaling peptide polymorphisms were associated with the early onset of Alzheimer's disease [46]. The TOMM40 was involved in protein degradation, apoptosis, neuronal loss and regulation of neural development [47]. The KLHL, CD101, HPCAL4, CRACD, OSBPL10, CFAP99, ECT2L, SGCZ, PDK1, VAV2, and NUP153 were expressed in the cerebral nervous system and associated with brain cortical structures, blood-brain barrier and cellular lipid metabolism. They played an important role in the functional pathways affected by AD. Immune dysregulation was clinically present in the brain and blood of Alzheimer's disease patients, which was associated with the expression of the HAO1 and PRF1 genes.

These genetic findings were benefit for the early diagnosis of AD. It may be difficult for family members and clinicians to detect abnormalities in patients for a long time before clinical symptoms of Alzheimer's disease appear. The asymptomatic individuals were at high risk of

developing Alzheimer's disease and should be continuously observed and prevented in advance. The imaging features of AD were derived from protein abnormalities, which were influenced by genetic and environmental factors. Variant genes STARD4, MME, MTRR, FRMD4A and TOMM40 might lead to pathological features of senile plaques, neuronal fiber tangles, hippocampal pyramidal cell granular vacuolar degeneration and neuronal deficits through protein expression. Therefore, the study of the susceptibility genes would be helpful to explore the underlying mechanisms of the disease. In addition, the lifestyle habits and environmental factors might interact with genetic and affect the risk of AD development. Specifically, Chronic cigarette smoking had been linked to increased rates of cognitive impairment [48] and structural abnormalities in the brain including alterations in cerebral white matter volume [49,50], and atrophy of gray matter structures in the temporal and parietal lobes [51]. Therefore, the environmental factors might be important in the initiation and promotion of the Alzheimer's disease.

Several limitations should be considered in this study. First, we only utilized the structural MRI instead of other modalities. Different types of brain imaging data contained different information. Therefore, the future work will focus on the findings of biomarkers in other types of brain imaging data and verifying the robustness of the model, such as fMRI, PET and DTI. Second, the brain atlases of different patient groups were various. Therefore, the model should be tested and improved on different patient groups such as different countries, nationalities, and ethnicities in order to evaluate the generalizability and reliability of the proposed method.

5. Conclusion

In this paper, we proposed the multi-channel feature fusion method based on CSES-NET for early AD diagnosis. The features from multiple image scales of sMRI were used in the fully connected networks for

classification which included deep features based on attention-based deep convolutional neural networks, radiomics features based on gray matter images and four cortical index features. The neuroimaging potential biomarkers associated with the disease may help physicians to make early diagnosis of AD. In addition, identification of risk loci can help the study of genes with functional genetic variation in the brain, which can provide important information for diagnosis and rational drug development in AD with early asymptomatic.

CRedit authorship contribution statement

Jianping Qiao: Conceptualization, Methodology, Software, Validation, Formal analysis, Writing – original draft, Writing – review & editing. **Mowen Zhang:** Conceptualization, Methodology, Software, Validation, Writing – original draft, Data curation, Writing – review & editing, Visualization. **Yanling Fan:** Resources, Writing – review & editing. **Kunlun Fang:** Software, Resources, Writing – review & editing. **Xiuhe Zhao:** Supervision, Writing – review & editing. **Shengjun Wang:** Supervision, Writing – review & editing. **Zhishun Wang:** Supervision, Writing – review & editing.

Declaration of Competing Interest

The authors declare that they have no known competing financial interests or personal relationships that could have appeared to influence the work reported in this paper.

Data availability

The authors do not have permission to share data.

Acknowledgments

This work was supported by the National Natural Science Foundation of China (61603225).

References

- [1] D.A. Butterfield, B. Halliwell, Oxidative stress, dysfunctional glucose metabolism and Alzheimer disease, *Nat. Rev. Neurosci.* 20 (3) (2019) 148–160, <https://doi.org/10.1038/s41583-019-0132-6>.
- [2] E. Mazrooei Rad, M. Azarnosh, M. Ghoshuni, M.M. Khalilzadeh, Diagnosis of mild Alzheimer's disease by EEG and ERP signals using linear and nonlinear classifiers, *Biomed. Signal Process. Control* 70 (2021), <https://doi.org/10.1016/j.bspc.2021.103049>.
- [3] P. Talwar, S. Kushwaha, M. Chaturvedi, V. Mahajan, Systematic Review of Different Neuroimaging Correlates in Mild Cognitive Impairment and Alzheimer's Disease, *Clin. Neurodiagn.* 31 (4) (2021) 953–967, <https://doi.org/10.1007/s00062-021-01057-7>.
- [4] W. Li, Z. Zhao, M. Liu, S. Yan, Y. An, L. Qiao, et al., Multimodal Classification of Alzheimer's Disease and Amnesic Mild Cognitive Impairment: Integrated 18F-FDG PET and DTI Study, *J. Alzheimers Dis.* 85 (3) (2022) 1063–1075, <https://doi.org/10.3233/JAD-215338>.
- [5] R. Hedayati, M. Khedmati, M. Taghipour-Gorjilolaie, Deep feature extraction method based on ensemble of convolutional auto encoders: Application to Alzheimer's disease diagnosis, *Biomed. Signal Process. Control* 66 (2021), <https://doi.org/10.1016/j.bspc.2020.102397>.
- [6] A. Basher, B.C. Kim, K.H. Lee, H.Y. Jung, Volumetric Feature-Based Alzheimer's Disease Diagnosis From sMRI Data Using a Convolutional Neural Network and a Deep Neural Network, *IEEE Access* 9 (2021) 29870–29882, <https://doi.org/10.1109/access.2021.3059658>.
- [7] S. Ahmed, B.C. Kim, K.H. Lee, H.Y. Jung, I. Alzheimer's Disease Neuroimaging, Ensemble of ROI-based convolutional neural network classifiers for staging the Alzheimer disease spectrum from magnetic resonance imaging, *PLoS One* 15 (12) (2020) e0242712.
- [8] W. Zhu, L. Sun, J. Huang, L. Han, D. Zhang, Dual Attention Multi-Instance Deep Learning for Alzheimer's Disease Diagnosis With Structural MRI, *IEEE Trans. Med. Imaging* 40 (9) (2021) 2354–2366, <https://doi.org/10.1109/TMI.2021.3077079>.
- [9] L. Tang, X. Wu, H. Liu, F. Wu, R. Song, W. Zhang, et al., Individualized Prediction of Early Alzheimer's Disease Based on Magnetic Resonance Imaging Radiomics, Clinical, and Laboratory Examinations: A 60-Month Follow-Up Study, *J Magn Reson Imaging* 54 (5) (2021) 1647–1657, <https://doi.org/10.1002/jmri.27689>.
- [10] S.G. Costafreda, I.D. Dinov, Z. Tu, Y. Shi, C.Y. Liu, I. Kloszewska, et al., Automated hippocampal shape analysis predicts the onset of dementia in mild cognitive impairment, *Neuroimage* 56 (1) (2011) 212–219, <https://doi.org/10.1016/j.neuroimage.2011.01.050>.
- [11] F. Feng, P. Wang, K. Zhao, B. Zhou, H. Yao, Q. Meng, et al., Radiomic Features of Hippocampal Subregions in Alzheimer's Disease and Amnesic Mild Cognitive Impairment, *Front. Aging Neurosci.* 10 (2018) 290, <https://doi.org/10.3389/fnagi.2018.00290>.
- [12] P. Hartikainen, J. Rasanen, V. Julkunen, E. Niskanen, M. Hallikainen, M. Kivipelto, et al., Cortical thickness in frontotemporal dementia, mild cognitive impairment, and Alzheimer's disease, *J. Alzheimers Dis.* 30 (4) (2012) 857–874, <https://doi.org/10.3233/JAD-2012-112060>.
- [13] S. Lahmiri, A. Shmuel, Performance of machine learning methods applied to structural MRI and ADAS cognitive scores in diagnosing Alzheimer's disease, *Biomed. Signal Process. Control* 52 (2019) 414–419, <https://doi.org/10.1016/j.bspc.2018.08.009>.
- [14] Z. Wu, Y. Peng, M. Hong, Y. Zhang, Gray Matter Deterioration Pattern During Alzheimer's Disease Progression: A Regions-of-Interest Based Surface Morphometry Study, *Front. Aging Neurosci.* 13 (2021), 593898, <https://doi.org/10.3389/fnagi.2021.593898>.
- [15] C.M. Karch, C. Cruchaga, A.M. Goate, Alzheimer's disease genetics: from the bench to the clinic, *Neuron* 83 (1) (2014) 11–26, <https://doi.org/10.1016/j.neuron.2014.05.041>.
- [16] T.M. Lancaster, M.J. Hill, R. Sims, J. Williams, Microglia - mediated immunity partly contributes to the genetic association between Alzheimer's disease and hippocampal volume, *BrainBehav. Immun.* 79 (2019) 267–273, <https://doi.org/10.1016/j.bbi.2019.02.011>.
- [17] J. Homann, T. Osburg, O. Ohlei, V. Dobricic, L. Deecke, I. Bos, et al., Genome-Wide Association Study of Alzheimer's Disease Brain Imaging Biomarkers and Neuropsychological Phenotypes in the European Medical Information Framework for Alzheimer's Disease Multimodal Biomarker Discovery Dataset, *Front. Aging Neurosci.* 14 (2022), 840651, <https://doi.org/10.3389/fnagi.2022.840651>.
- [18] L.V. Fulton, D. Dolezel, J. Harrop, Y. Yan, C.P. Fulton, Classification of Alzheimer's Disease with and without Imagery using Gradient Boosted Machines and ResNet-50, *BrainSci.* 9 (9) (2019), <https://doi.org/10.3390/brainsci9090212>.
- [19] Y. Chen, An Alzheimer's Disease Identification and Classification Model Based on the Convolutional Neural Network with Attention Mechanisms, *Traitement du Signal* 38 (5) (2021) 1557–1564, <https://doi.org/10.18280/ts.380533>.
- [20] J. Zhang, Y. Gao, Y. Gao, B.C. Munsell, D. Shen, Detecting Anatomical Landmarks for Fast Alzheimer's Disease Diagnosis, *IEEE Trans. Med. Imaging* 35 (12) (2016) 2524–2533, <https://doi.org/10.1109/TMI.2016.2582386>.
- [21] Z. Xiao, Y. Ding, T. Lan, C. Zhang, C. Luo, Z. Qin, Brain MR Image Classification for Alzheimer's Disease Diagnosis Based on Multifeature Fusion, *Comput. Math Methods Med.* 2017 (2017) 1952373, <https://doi.org/10.1155/2017/1952373>.
- [22] M. Liu, J. Zhang, D. Nie, P.T. Yap, D. Shen, Anatomical Landmark Based Deep Feature Representation for MR Images in Brain Disease Diagnosis, *IEEE J. Biomed. Health Inform.* 22 (5) (2018) 1476–1485, <https://doi.org/10.1109/JBHI.2018.2791863>.
- [23] C. Lian, M. Liu, J. Zhang, D. Shen, Hierarchical Fully Convolutional Network for Joint Atrophy Localization and Alzheimer's Disease Diagnosis Using Structural MRI, *IEEE Trans Pattern Anal. Mach. Intell.* 42 (4) (2020) 880–893, <https://doi.org/10.1109/TPAMI.2018.2889096>.
- [24] Yue Wu, Taoran Li, Ying Han, & Jiang., J. (2020). Use of radiomic features and support vector machine to discriminate subjective cognitive decline and healthy controls. 2020 42nd Annual International Conference of the IEEE Engineering in Medicine & Biology Society (EMBC), 1762-1765. <https://doi.org/10.1109/EMBC44109.2020.9175840>.
- [25] F. Li, M. Liu, I. Alzheimer's Disease Neuroimaging, Alzheimer's disease diagnosis based on multiple cluster dense convolutional networks, *Comput. Med. Imaging Graph* 70 (2018) 101–110, <https://doi.org/10.1016/j.compmedimag.2018.09.009>.
- [26] K. Hett, V.T. Ta, G. Catheline, T. Tourdias, J.V. Manjon, P. Coupe, I. Alzheimer's Disease Neuroimaging, Multimodal Hippocampal Subfield Grading For Alzheimer's Disease Classification, *Sci. Rep.* 9 (1) (2019) 13845, <https://doi.org/10.1038/s41598-019-49970-9>.
- [27] R. Cui, M. Liu, Hippocampus Analysis by Combination of 3-D DenseNet and Shapes for Alzheimer's Disease Diagnosis, *IEEE J. Biomed. Health Inform.* 23 (5) (2019) 2099–2107, <https://doi.org/10.1109/JBHI.2018.2882392>.
- [28] M. Liu, D. Zhang, D. Shen, Relationship Induced Multi-Template Learning for Diagnosis of Alzheimer's Disease and Mild Cognitive Impairment, *IEEE Trans. Med. Imaging* 35 (6) (2016) 1463–1474, <https://doi.org/10.1109/TMI.2016.2515021>.
- [29] L. Zhan, Y. Liu, J. Zhou, & Ye., J. (2015). Boosting classification accuracy of diffusion MRI derived brain networks for the subtypes of mild cognitive impairment using higher order singular value decomposition. *IEEE 12th International Symposium on Biomedical Imaging (ISBI)*, 131-135. <https://doi.org/10.1109/ISBI.2015.7163833>.
- [30] G. Prasad, S.H. Joshi, T.M. Nir, A.W. Toga, P.M. Thompson, I. Alzheimer's Disease Neuroimaging, Brain connectivity and novel network measures for Alzheimer's disease classification, S121-131, *Neurobiol. Aging* 36 (Suppl 1) (2015), <https://doi.org/10.1016/j.neurobiolaging.2014.04.037>.
- [31] M. La Rocca, N. Amoroso, A. Monaco, R. Bellotti, S. Tangaro, A novel approach to brain connectivity reveals early structural changes in Alzheimer's disease, *Physiol. Meas.* 39 (7) (2018), 074005, <https://doi.org/10.1088/1361-6579/aacflf>.
- [32] M. Shakeri, H. Lombaert, S. Tripathi, S. Kadoury, Deep Spectral-Based Shape Features for Alzheimer's Disease Classification, Spectral and Shape Analysis in Medical Imaging, *Cham* (2016) 15–24, https://doi.org/10.1007/978-3-319-51237-2_2.

- [33] C. McDonald, L. McEvoy, L. Gharapetian, C. Fennema-Notestine, D. Hagler, D. Holland, et al., Regional rates of neocortical atrophy from normal aging to early Alzheimer disease, *Neurology* 73 (6) (2009) 457–465, <https://doi.org/10.1212/WNL.0b013e3181b16431>.
- [34] V. Singh, H. Chertkow, J.P. Lerch, A.C. Evans, A.E. Dorr, N.J. Kabani, Spatial patterns of cortical thinning in mild cognitive impairment and Alzheimer's disease, *Brain* 129 (Pt 11) (2006) 2885–2893, <https://doi.org/10.1093/brain/awl256>.
- [35] E. Dicks, L. Vermunt, W.M. van der Flier, P.J. Visser, F. Barkhof, P. Scheltens, et al., Modeling grey matter atrophy as a function of time, aging or cognitive decline show different anatomical patterns in Alzheimer's disease, *Neuroimage Clin.* 22 (2019), 101786, <https://doi.org/10.1016/j.nicl.2019.101786>.
- [36] Z. Moussavi, Repetitive TMS applied to the precuneus stabilizes cognitive status in Alzheimer's disease, *Brain* 145 (11) (2022) 3730–3732, <https://doi.org/10.1093/brain/awac285>.
- [37] J. Antczak, G. Rusin, A. Slowik, Transcranial Magnetic Stimulation as a Diagnostic and Therapeutic Tool in Various Types of Dementia, *J Clin Med* 10 (13) (2021), <https://doi.org/10.3390/jcm10132875>.
- [38] S. Salunkhe, M. Bachute, S. Gite, N. Vyas, S. Khanna, K. Modi, et al., Classification of Alzheimer's Disease Patients Using Texture Analysis and Machine Learning. *Applied System, Innovation* 4 (3) (2021), <https://doi.org/10.3390/asi4030049>.
- [39] X. Hao, Y. Bao, Y. Guo, M. Yu, D. Zhang, S.L. Risacher, et al., Multi-modal neuroimaging feature selection with consistent metric constraint for diagnosis of Alzheimer's disease, *Med. Image Anal.* 60 (2020), 101625, <https://doi.org/10.1016/j.media.2019.101625>.
- [40] O. Hansson, R.M. Edelmayer, A.L. Boxer, M.C. Carrillo, M.M. Mielke, G. D. Rabinovici, et al., The Alzheimer's Association appropriate use recommendations for blood biomarkers in Alzheimer's disease, *Alzheimers Dement* 18 (12) (2022) 2669–2686, <https://doi.org/10.1002/alz.12756>.
- [41] T. Nikolai, F. Dechterenko, B. Yaffe, H. Georgi, M. Kopecek, M. Cervenkova, et al., Reducing misclassification of mild cognitive impairment based on base rate information from the uniform data set, *Aging Neuropsychol. Cogn.* (2022), <https://doi.org/10.1080/13825585.2021.2022593>.
- [42] F. Gao, Integrated Positron Emission Tomography/Magnetic Resonance Imaging in clinical diagnosis of Alzheimer's disease, *Eur. J. Radiol.* 145 (2021), 110017, <https://doi.org/10.1016/j.ejrad.2021.110017>.
- [43] B. Mesmin, N.H. Pipalia, F.W. Lund, T.F. Ramlall, A. Sokolov, D. Eliezer, F. R. Maxfield, STARD4 abundance regulates sterol transport and sensing, *Mol. Biol. Cell* 22 (21) (2011) 4004–4015, <https://doi.org/10.1091/mbc.E11-04-0372>.
- [44] A. Stocco, P. Tannorella, L. Migliore, F. Coppede, Polymorphisms of genes required for methionine synthesis and DNA methylation influence mitochondrial DNA methylation, *Epigenomics* 12 (12) (2020) 1003–1012, <https://doi.org/10.2217/epi-2020-0041>.
- [45] X. Yan, N.P. Nykanen, C.A. Brunello, A. Haapasalo, M. Hiltunen, R.L. Uronen, H. J. Huttunen, FRMD4A-cytohesin signaling modulates the cellular release of tau, *J. Cell Sci.* 129 (10) (2016) 2003–2015, <https://doi.org/10.1242/jcs.180745>.
- [46] A. Sanchez-Navarro, I. Gonzalez-Soria, R. Caldino-Bohn, N.A. Bobadilla, An integrative view of serpins in health and disease: the contribution of SerpinA3, C106-C118, *Am. J. Physiol. Cell Physiol.* 320 (1) (2021), <https://doi.org/10.1152/ajpcell.00366.2020>.
- [47] A.J. Saykin, L. Shen, T.M. Foroud, S.G. Potkin, S. Swaminathan, S. Kim, et al., Alzheimer's Disease Neuroimaging Initiative biomarkers as quantitative phenotypes: Genetics core aims, progress, and plans, *Alzheimers Dement* 6 (3) (2010) 265–273, <https://doi.org/10.1016/j.jalz.2010.03.013>.
- [48] T.C. Durazzo, S. Gazdzinski, D.J. Meyerhoff, The neurobiological and neurocognitive consequences of chronic cigarette smoking in alcohol use disorders, *Alcohol Alcohol.* 42 (3) (2007) 174–185, <https://doi.org/10.1093/alcalc/ags020>.
- [49] J.J. Wang, T.C. Durazzo, S. Gazdzinski, P.H. Yeh, A. Mon, D.J. Meyerhoff, MRSI and DTI: a multimodal approach for improved detection of white matter abnormalities in alcohol and nicotine dependence, *NMR Biomed.* 22 (5) (2009) 516–522, <https://doi.org/10.1002/nbm.1363>.
- [50] S. Gazdzinski, T.C. Durazzo, C. Studholme, E. Song, P. Banys, D.J. Meyerhoff, Quantitative Brain MRI in Alcohol Dependence: Preliminary Evidence for Effects of Concurrent Chronic Cigarette Smoking on Regional Brain Volumes, *Alcohol: Clin. Exp. Res.* 29 (8) (2005) 1484–1495, <https://doi.org/10.1097/01.alc.0000175018.72488.61>.
- [51] H.C. Fritz, K. Wittfeld, C.O. Schmidt, M. Domin, H.J. Grabe, K. Hegenscheid, N. Hosten, M. Lotze, Current smoking and reduced gray matter volume—a voxel-based morphometry study, *Neuropsychopharmacology* 39 (11) (2014) 2594–2600, <https://doi.org/10.1038/npp.2014.112>.